



1 **Microphysical properties of various precipitation systems worldwide**  
2 **classified via objective methods based on dual-frequency**  
3 **precipitation radar observations**

4 Yujia Zhang<sup>1,2</sup> Xiaodong Zhang<sup>1,2</sup>, Xiang Ni<sup>1,2</sup>

5 <sup>1</sup>Chongqing Jinmo Mountain Karst Ecosystem National Observation and Research Station, School of Geographical Sciences,  
6 Southwest University, Chongqing, China

7 <sup>2</sup>Chongqing Engineering Research Center for Remote Sensing Big Data Application, School of Geographical Sciences,  
8 Southwest University, Chongqing, China

9 *Correspondence to:* Xiang Ni (nixiang@swu.edu.cn)



11 **Abstract.** Microphysical properties play crucial roles in physical processes related to the development of precipitation. In  
12 this study, Global Precipitation Measurement (GPM) dual-frequency precipitation radar (DPR) data were processed to  
13 demonstrate the microphysical properties of different precipitation systems (PSs) that are objectively classified with the k-  
14 means clustering algorithm. Four types of regular/non-extreme PS (high-latitude shallow PS, subtropical shallow PS,  
15 moderate PS, deep PS) and four types of extreme PS (extreme deep PS, strong PS, extreme strong PS, and marine extreme  
16 PS) were recognized. These eight types of PS exhibit differences in spatial-temporal features and convection characteristics,  
17 such as storm height, rain intensity, and vertical structures. For example, with the highest radar echo top and the largest mean  
18 mass-weighted mean diameter ( $D_m$ ), the extreme strong PS mainly locate over tropical continent, while the high-latitude  
19 shallow PS have the least precipitation rate and mean normalized intercept parameter ( $N_w$ ) values. The relationships between  
20 convection features and microphysical properties also vary among the eight types of PSs. For extreme PS, maximum  
21 precipitation rate near the surface generally exceeds 100 mm h<sup>-1</sup> and balanced breakup and coalescence processes play a  
22 dominant role compared with non-extreme PS. In contrary, the coalescence processes dominate near the surface in two types  
23 of shallow PS. These results highlight the diversity of global precipitation microphysics and emphasize the necessity of  
24 global studies to increase the understanding of precipitation processes.

25



## 26 1. Introduction

27 The microphysical characteristics of precipitation provide crucial information for describing precipitation. The deficiency of  
28 precipitation microphysical parameterization schemes is a significant factor contributing to precipitation errors in weather  
29 and climate models (Snook and Xue, 2008). Accurately obtaining spatial and temporal distributions and variations in  
30 precipitation microphysical parameters is essential for understanding the physical processes of precipitation, increasing the  
31 accuracy of quantitative precipitation estimation (QPE), and evaluating microphysical parameterizations in models (Chen et  
32 al., 2011; Zhang et al., 2023). Currently, observations and characteristics of precipitation microphysics at the global scale  
33 remain lacking because of the limited number of observation approaches.

34 The drop size distribution (DSD) is a typical metric for depicting precipitation microphysics. DSD features can be derived  
35 from observations obtained via disdrometers, ground-based radar instruments, and space-based radar instruments. In radar  
36 instruments, the interaction of electromagnetic waves with hydrometeors is used to retrieve DSD parameters (Marzuki et al.,  
37 2023), whereas disdrometers measure raindrop counts to directly obtain DSDs at the surface. Disdrometers provide only  
38 point measurements at specific levels and cannot measure the vertical structure of DSDs. Moreover, disdrometers have not  
39 been deployed globally, especially over the ocean. Although ground-based radar instruments can measure the three-  
40 dimensional structure of precipitation, they can only be used in limited areas, and their observation accuracy is significantly  
41 affected by the terrain conditions within the observation area (Dai et al., 2020). In contrast, space-based radar instruments  
42 can provide the vertical structures of DSD parameters worldwide. This study focused on the microphysical characteristics of  
43 various precipitation systems (PSs) worldwide. Compared with other instruments, space-based radar instruments are the  
44 most suitable for researching global precipitation microphysics.

45 In 1997, the Tropical Rainfall Measuring Mission (TRMM) satellite was launched by the National Aeronautics and Space  
46 Administration (NASA) and the Japan Aerospace Exploration Agency (JAXA). The precipitation radar (PR), which operates  
47 in the Ku-band (13.8 GHz), was carried by the TRMM (Iguchi et al., 2000). This marked the beginning of the observation of  
48 precipitation microphysics via space-based radar instruments. Notably, DSD parameters were retrieved from the radar  
49 reflectivity measured by the PR with the assumption that the DSD can be characterized by the diameter parameter itself  
50 (Iguchi et al., 2000). As a result, the DSDs obtained via retrieval exhibited large errors. In 2014, NASA and JAXA  
51 successfully launched the Global Precipitation Measurement (GPM) Core Observatory (GPM-CO). The GPM-CO carried  
52 the first spaceborne dual-frequency precipitation radar (DPR) system, operating in the Ku and Ka bands (13 and 35 GHz,  
53 respectively) (Skofronick-Jackson et al., 2017). The differential scattering during rainfall at these two frequencies is directly  
54 related to the size of raindrops (Gatlin et al., 2020). Via the use of this characteristic,  $D_m$  and  $N_w$  can be retrieved. The  
55 retrieved DSD parameters have been verified with ground-based observations and are better than those obtained via the  
56 TRMM PR algorithm (Sun et al., 2020). In addition, validation studies have confirmed the feasibility of using DPR  
57 observations for DSD parameter analysis (D'Adderio et al., 2018; Peinó et al., 2024). Peinó et al. (2024) used observational  
58 data from seven Parsivel disdrometers across different topographic zones in the western Mediterranean to validate GPM



59 DSD products. They reported that the GPM DPR products effectively captured the variations in DSDs observed under  
60 different rainfall intensities. Therefore, GPM DSD products have been widely employed to investigate the microphysical  
61 characteristics of precipitation in the literature (Wen et al., 2024, 2023).

62 However, previous studies involving GPM DSD products have focused mainly on specific locations or weather systems. For  
63 example, Li et al. (2024) studied the vertical structure and DSD characteristics of different precipitation types during the  
64 rainy season over South China and reported that the precipitation type and intensity affect the DSD parameters. In their study,  
65 under the same precipitation intensity, shallow convective precipitation exhibited the smallest  $D_m$  and largest  $N_w$  values,  
66 whereas deep convective precipitation exhibited the opposite phenomenon. Additionally, regarding stratiform precipitation,  
67 for  $PR > 3.5 \text{ mm h}^{-1}$ ,  $D_m$  slightly increased, and in regard to shallow convective precipitation,  $D_m$  remained at approximately  
68 1.3 mm for  $PR > 2 \text{ mm h}^{-1}$ . Similarly, Wen et al. (2023) analyzed the seasonal variations in the vertical structure of  
69 precipitation microphysics in East China. They reported that the spatial distributions of  $D_m$  and  $N_w$  demonstrate obvious  
70 seasonal variations and that there are more small raindrops in convective precipitation in autumn and winter than during the  
71 other seasons. These studies revealed the variations in microphysical characteristics across different seasons and rainfall  
72 types. Additionally, regarding weather conditions, regional variations in the precipitation characteristics of tropical cyclones  
73 (TCs) have been investigated over the North Indian Ocean (Kumar et al., 2023). Research has revealed that the nature of  
74 microphysical processes largely influences the growth of droplets in convective and stratiform rain. Wu et al. (2022)  
75 investigated the DSD characteristics of record-breaking Typhoon In-Fa (2021). Their findings revealed significant internal  
76 and regional differences in the microphysical characteristics of typhoon precipitation. When different precipitation types  
77 during Typhoon In-Fa were compared, convective precipitation ( $N_w$  values ranging from  $3.80$  to  $3.96 \text{ m}^{-3} \text{ mm}^{-1}$ ) exhibited  
78 higher raindrop concentrations than did stratiform precipitation ( $N_w$  values ranging from  $3.40$  to  $3.50 \text{ m}^{-3} \text{ mm}^{-1}$ ).  
79 Additionally, convective precipitation during Typhoon In-Fa indicated a greater (lower) raindrop concentration than that  
80 during Typhoon Taiwan (Hainan), while the raindrop diameter was smaller than those during both Typhoons Taiwan and  
81 Hainan. These studies primarily focused on the microphysical process and structure of various weather conditions, which  
82 provided insight into the formation process of precipitation. At present, there are few studies on the microphysical  
83 characteristics of large-scale and global PSs. On the one hand, as mentioned above, the DSD is influenced by numerous  
84 factors, such as precipitation type and season. There may be multiple precipitation types and DSDs in one area. On the other  
85 hand, few DSD datasets covering the whole world are available. Dolan et al. (2018) used twelve disdrometer datasets across  
86 three latitudinal zones—high-latitude, midlatitude, and low-latitude zones—to analyze DSD spatial variability. They  
87 reported that the DSD varies with latitude. At low latitudes, moderate  $D_m$  values (1.5–2 mm) and large  $\log_{10}(N_w)$  values ( $> 4$   
88  $\text{m}^{-3} \text{ mm}^{-1}$ ) dominated. At midlatitudes, high  $D_m$  values and small  $N_w$  values dominated. At high latitudes, low  $D_m$  and large  
89  $N_w$  values prevailed. Although the dataset covered a wide range of precipitation regimes, it could not capture all rain regimes.  
90 Moreover, a regional DSD dataset cannot represent the DSD within a given latitudinal band because of the limitations of  
91 disdrometers. Hence, in this study, GPM DSD products were employed to investigate the microphysical characteristics of  
92 PSs at global scales.



93 This study aimed to classify different PSs on the basis of DPR observations via machine learning and to analyze the  
94 microphysical characteristics of different types of PSs. The results could address regional DSD variability and increase our  
95 understanding of the microphysical processes of different types of PSs. This study is organized in four sections. Section 2  
96 provides detailed descriptions of the GPM data and machine learning models applied in this study. The main results are  
97 presented in Section 3, and finally, a summary is given in Section 4.

98 **2. Data and methods**

99 **2.1. Data**

100 GPM observations cover the range from 65° S to 65° N (Hou et al., 2014; Tapiador et al., 2012). The GPM DPR operates in  
101 the Ka and Ku bands, with a spatial resolution of approximately  $5 \times 5 \text{ km}^2$ . The scanning of DPR is cross-track and has three  
102 scan patterns: normal scanning (NS), matching scanning (MS), and high sensitivity scanning (HS) (Das et al., 2022). Since  
103 the scanning pattern of the Ka-band was changed in 2018 (Awaka et al., 2021), the GPM 2A DPR (version 7) products  
104 considered the changes in the Ka-band scan pattern with a more accurate precipitation estimation algorithm. The product  
105 formats in version 7 have been changed from the original three types to two types: FS and HS. The FS product exhibits a  
106 new format and is defined as a full-scan dual-frequency product with a 125-m distance resolution. Compared with previous  
107 algorithms, the FS mode makes it possible for the first time to process a full-scan band of approximately 245 km in dual-  
108 band mode (Awaka et al., 2021). Therefore, the FS type was adopted in this study.

109 In this study, five years (2018–2022) of 2A DPR products (version 7) were employed. The parameters used in this machine  
110 learning model include DSD parameters ( $D_m$  and  $N_w$ ), near-surface precipitation rate ( $\text{mm h}^{-1}$ ), attenuation-corrected radar  
111 reflectivity (dBZ), reflectivity near the surface ( $Z_{\text{surf}}$ ), and typeprecip (stratiform and convective precipitation pixels are  
112 distinguished by the typeprecip parameter), and airTemperature (this parameter can be used to distinguish between snow and  
113 rain).

114 **2.2. Precipitation system (PS)**

115 This paper presents a method based on the connected domain principle for identifying PSs similar to those contained in the  
116 widely used TRMM/GPM Precipitation Feature dataset (Liu et al., 2008, 2020). Similar to the Precipitation Feature dataset  
117 (Liu et al., 2008), neighboring precipitation pixels, with a minimum precipitation rate of  $0.1 \text{ mm h}^{-1}$ , are grouped into a PS.  
118 Each PS is required to have a minimum of four precipitation pixels.

119 The DPR can observe the three-dimensional structure of precipitation and DPR products include radar reflectivity  
120 parameters and retrieved DSD parameters from 0 to 22 km with a range resolution of 125 m, resulting in a total of 176 layers  
121 of data. Consequently, for each PS type, DSD and radar reflectivity parameters such as the maximum and average values of  
122 each layer were calculated. The average  $D_m$  and  $N_w$  profiles were used for each PS, and if the profiles of the maximum  $D_m$   
123 and  $N_w$  values in each layer were involved, MAX- $D_m$  and MAX- $N_w$ , respectively, were used. Given the potential



relationships of the convective intensity with microphysical parameters,  $Z_e$  in the product was employed to calculate the maximum 20/30/40 dBZ echo top height (MAXHT20/30/40) for each type of PS (Liu, 2011; Liu et al., 2020; Ni et al., 2019; Roy et al., 2020), the echo top height of the PS ( $H_{top}$ ) (Arulraj and Barros, 2021), and other convective parameters. To characterize the conditions of the PS, several additional features were calculated, such as the maximum precipitation rate near the surface (the maximum precipitation rate of the precipitation pixels included in the PS) and the precipitation area (the number of precipitation pixels contained in the PS). Considering that the GPM satellite exhibits a higher observation frequency in high-latitude regions (approximately 2–3 times that at the equator), the original dataset is prone to oversampling in these areas, which can introduce bias. To construct a balanced dataset suitable for clustering analysis, this study implemented a homogenization for the sampling. Specifically, the satellite's observation frequency was calculated as a function of latitude, and sample size for each latitude was adjusted using the ratio of its frequency to that at the equator. Subsequently, precipitation systems were randomly selected from each latitude to ensure a consistent scaled sample size, thereby effectively addressing the issue of uneven sampling. Finally, a total of 8,924,307 PSs were obtained for subsequent analysis.

### 2.3. Methods

In this study, two distinct machine learning models, namely k-means clustering and principal component analysis (PCA) were used. Both models were trained and evaluated via the Python scikit-learn package. These models are briefly described below. The k-means algorithm is one of the most popular clustering algorithms among machine learning algorithms. It is one of the most popular unsupervised clustering algorithms due to its efficiency (Jain, 2010). The algorithm follows a three-step process. Initially, it aims to select initial cluster centers by randomly obtaining sample coordinates from the dataset and assigning each sample to its nearest cluster center. Next, it computes the mean of all sample points assigned to each previous cluster center to establish new cluster centers. Finally, the algorithm aims to evaluate the differences between the new and old cluster centers. If differences are present, the last two steps are repeated until the cluster centers stabilize and no longer shift (Jain, 2010).

PCA is a classical dimensionality reduction tool in machine learning (Gang and Bajwa, 2022). PCA is based on the linear combination of target features to construct the principal subspace, and the variance is then employed to measure the information content with the aim of identifying the linear subspace with the maximum variance (Marukatat, 2023). In summary, PCA aims to transform numerous pertinent features into a comparatively limited number of irrelevant ones, thereby retaining as much of the informational content of the original data as possible (Gang and Bajwa, 2022). Considering that there are 176 vertical layers of GPM DPR products, if all DSD data were used as input parameters, the clustering effect could be poor because of the high dimensionality. In this study, PCA was adopted to reduce the dimensionality of the data while striking a balance between information loss and the optimal number of parameters to be retained (Festa et al., 2023; Jolliffe and Cadima, 2016).



156 In this study, the maximum precipitation rate near the surface,  $H_{top}$ , the precipitation area, the proportion of stratiform  
157 precipitation, the proportion of convective precipitation, the DSD parameters ( $D_m$  and  $N_w$ ) and the maximum radar  
158 reflectivity parameter ( $Z_e$ ) after dimensionality reduction via PCA were used as input parameters for the k-means clustering  
159 algorithm. These parameters were selected based on their critical role in comprehensively characterizing the features,  
160 structure, and microphysical processes of precipitation systems. Among them, the maximum surface precipitation rate and  $Z_e$   
161 reflect the intensity of the precipitation process and its echo characteristics, while the precipitation area directly characterizes  
162 the spatial differences in both the vertical and horizontal distributions of the system. The  $H_{top}$  not only reveals the vertical  
163 distribution but also captures the top-level information of the precipitation cloud through the maximum reflectivity height.  
164 Introducing the proportions of stratiform and convective precipitation facilitates the differentiation of precipitation types  
165 generated by distinct mechanisms, thereby elucidating their evolution patterns and dynamic characteristics. Furthermore, the  
166 DSD parameters ( $D_m$  and  $N_w$ ) effectively describe the size distribution of precipitation particles and their intrinsic physical  
167 processes, providing an essential basis for an in-depth understanding of precipitation microphysics. Collectively,  
168 constructing a multidimensional precipitation feature space with these parameters enhances the accuracy and robustness of  
169 the clustering analysis.

170 The quality of clustering was evaluated by analyzing different clustering structures derived from the same dataset. The most  
171 commonly employed performance metrics, such as the sum of squared errors (SSE), Davis Bouldin (DB) index, Calinski-  
172 Harabasz (CH) Score (El Khattabi et al., 2024) and silhouette index, can be utilized to assess the effectiveness and quality of  
173 clustering algorithms (Ay et al., 2023). In this case, the DB index was calculated by computing the average sum of the  
174 intraclass distances between any two clusters divided by the distance between the centers of those two clusters and obtaining  
175 the maximum value. The DB index can manage clusters of different sizes and densities with a high degree of robustness to  
176 noise and outliers.

177 The DB index is calculated by computing the average sum of intraclass distances between clusters, divided by the distance  
178 between their respective centers, with the final value determined by the maximum across all clusters. A lower DB index  
179 indicates better clustering performance (Sowan et al., 2023). Additionally, the CH score, which assesses clustering  
180 compactness and separation, was also considered. Higher CH scores indicate better-defined clusters. Algorithms with  
181 clustering numbers ranging from 3 to 20 were executed, and the resulting change in the DB index and CH score was plotted  
182 (refer to Fig. S1 in the Supplementary Material). The results show that when  $K = 8$ , the DB index reaches its lowest value,  
183 while the CH score remains relatively high, indicating a well-balanced clustering structure. Therefore, the optimal number of  
184 clusters is eight. Combining all the features of the PSs described in Section 3, the Cluster 1-8 could be regarded as four non-  
185 extreme PS (high-latitude shallow PS, subtropical shallow PS, moderate PS, deep PS) and four extreme PS (extreme deep PS,  
186 strong PS, extreme strong PS, and marine extreme PS), which are listed here for the convenience of understanding the  
187 following context.



188 **3. Results and discussion**

189 **3.1. Global distributions**

190 Table 1 shows the statistics of various parameters for the eight types of PS. There numbers include abundant information and  
191 verify the rationality of the objectively clustering algorithm. First, the numbers of the various types of PSs differed  
192 significantly. The two types of shallow PSs (high-latitude shallow PS and subtropical shallow PS) accounted for 81.44% of  
193 the total PS count. The proportions of deep and moderate PSs were 2.41% and 15.50%, respectively. The other four types of  
194 PS are regarded as extreme PS (extreme deep PS, strong PS, extreme strong PS, and marine extreme PS) because their ratios  
195 of the total PS are less than 1%, accounted for only 0.39%, 0.22%, 0.02%, and 0.01%, respectively. In the non-extreme PS,  
196 MAXHT20 is generally positively related to the precipitation rate (Table 1). However, in the extreme PS, the correlation  
197 between the extreme precipitation rate and MAXHT20 is not clear. For example, that the mean value of the maximum  
198 precipitation rate in marine extreme PS was the highest among the eight types of PSs, although its MAXHT20 was less than  
199 that in extreme strong PS and close to that in extreme deep PS. This result is consistent with other studies noting a weak link  
200 between the heaviest rainfall and the highest storm top (Hamada et al., 2015). Although the convective intensity of extreme  
201 deep PS is not significantly higher than that of deep PS, it exhibits a substantially larger precipitation area and maximum  
202 precipitation rate.

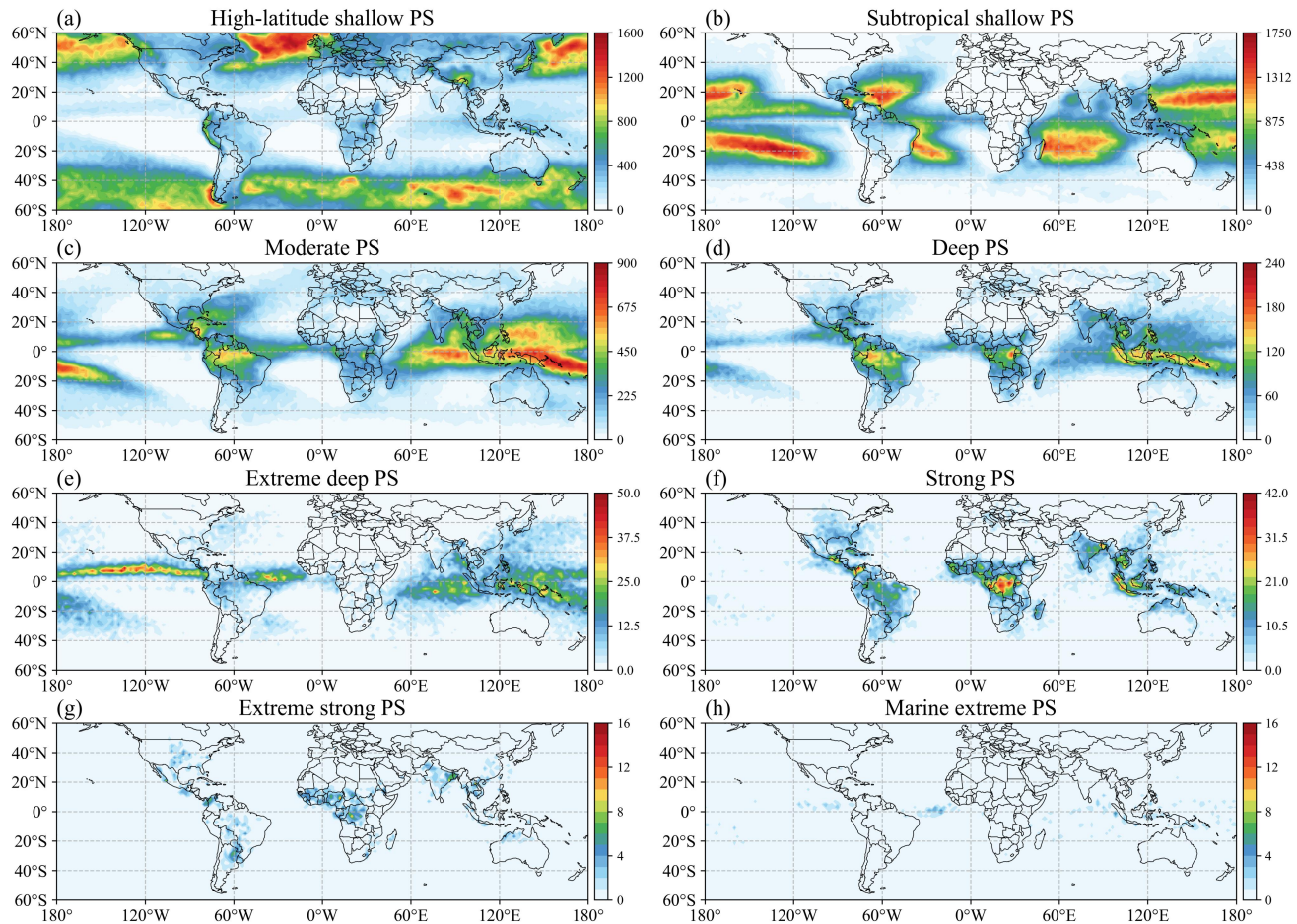
203 High-latitude shallow PS was most prevalent at midlatitudes and high latitudes, where snowfall and sleet are more  
204 frequent than at low latitudes. Notably, high-latitude shallow PS were dominated by stratiform precipitation, with stratiform  
205 pixels accounting for 88.63%. Meanwhile, approximately 86.60% of the PS exhibited surface temperatures higher than 0 °C.  
206 A study confirmed that at high latitudes and in polar regions, more than 25% of precipitation falls as snow (Lerber et al.,  
207 2018). This is consistent with the observations from high-latitude shallow PS. Additionally, an analysis of high-latitude  
208 shallow PS by latitude revealed that with increasing latitude, the number of samples generally increased. Moreover, the  
209 number of PSs with echo top heights less than 2.5 km increased with latitude. During the winter season at 65°S, PSs with  
210 echo top heights below 2.5 km accounted for approximately 50% of the total PSs there. This is likely due to the influence of  
211 the low surface temperature and weak convection (refer to Fig. S2 in the Supplementary Material).

212 Subtropical shallow PS primarily occurred over the ocean where is dominated by the subtropical high, with a relatively  
213 limited degree of overlap with moderate PS and deep PS (Fig. 1). The mean MAXHT20 value in subtropical shallow PS was  
214 only 3.29 km, and the proportion of convective precipitation was the highest among all the types of PSs, exceeding 90%.  
215 Compared with those of the other PSs, subtropical shallow PS exhibited the smallest precipitation area. Moreover, it was  
216 rarely found over land. These results support the conclusion that subtropical shallow PS is associated with isolated shallow  
217 convection over the ocean, which has been the topic of interest in previous studies (Chen and Liu, 2016; Chudler et al., 2022;  
218 Houze Jr. et al., 2015).

219 The geographic distribution patterns of deep PS and moderate PS were approximately the same (Fig. 1). The number of  
220 occurrences in the maritime continent (MC), Indian Ocean, Atlantic Ocean, Amazon rainforests and Pacific Ocean were



221 relatively high. There regions are generally influenced by the Intertropical Convergence Zone (ITCZ). Nevertheless, the deep  
222 PS has higher land percentage. The mean values of the maximum precipitation rates in moderate PS and deep PS were 6.21,  
223 35.94 mm h<sup>-1</sup>, respectively, whereas those of MAXHT20 were 7.03 and 11.89 km, respectively.  
224 Strong PS, extreme deep PS, extreme strong PS, and marine extreme PS demonstrated low sample sizes. However, their  
225 precipitation areas are significantly larger than non-extreme PS (Table 1). The location of extreme deep PS is similar with  
226 moderate and deep PS, with larger values for most parameters. In the extreme strong PS, the proportion of land pixels  
227 reaches 81%, with significant concentrations in near-equatorial Africa, America, India, the southeastern U.S., and South  
228 America. The average maximum precipitation rate in extreme strong PS was 156.37 mm h<sup>-1</sup>, and MAXHT40 reached 12.32  
229 km, which is the highest among all the types of PSs. The high MAXHT40 value indicates strong updraft in the middle  
230 troposphere, which is favorable for hailstone formation. Therefore, the spatial distributions of hailstorms in extreme strong  
231 PS were very similar to those of hailstorms with large hailstones on the ground (Marra et al., 2017). Marine extreme PS was  
232 primarily situated in the near-equatorial marine region, with only 943 PSs and 90% is over the ocean. The mean maximum  
233 precipitation rate in marine extreme PS was 178.30 mm h<sup>-1</sup>, ranking first among the eight types of PSs. Although the  
234 MAXHT20 value in marine extreme PS reached 12.81 km, the MAXHT40 value in marine extreme PS was approximately  
235 half of that in extreme strong PS, indicating low convection activity in the middle and upper levels. Oceanic extreme PS  
236 (extreme deep PS and marine extreme PS) with a high fraction of ocean pixels, exhibit a significantly larger precipitation  
237 coverage area than continental extreme PS (strong PS and extreme strong PS). This spatial distribution aligns with previous  
238 findings that the most extensive PS are predominantly located in oceanic regions. Furthermore, continental extreme PS  
239 display markedly stronger convective intensity. This disparity is largely attributable to the observation that the heaviest PS  
240 generally occur over tropical land, the Western Pacific warm pool, the North American Great Plains, and Argentina, whereas  
241 the most severe convective storms are predominantly observed over continental areas (Liu and Zipser, 2015).



242

243 **Figure 1.** Spatial distributions ( $2^\circ \times 2^\circ$ ) of the PS counts from 2018 to 2022

244



245 **Table 1.** Precipitation parameters for the different types of PSs. (\* indicate that in high-latitude shallow PS and  
246 subtropical shallow PS, approximately 80% of the samples do not reach 40 dBZ. Therefore, the mean MAXHT40 for these  
247 samples is recorded as 0.)

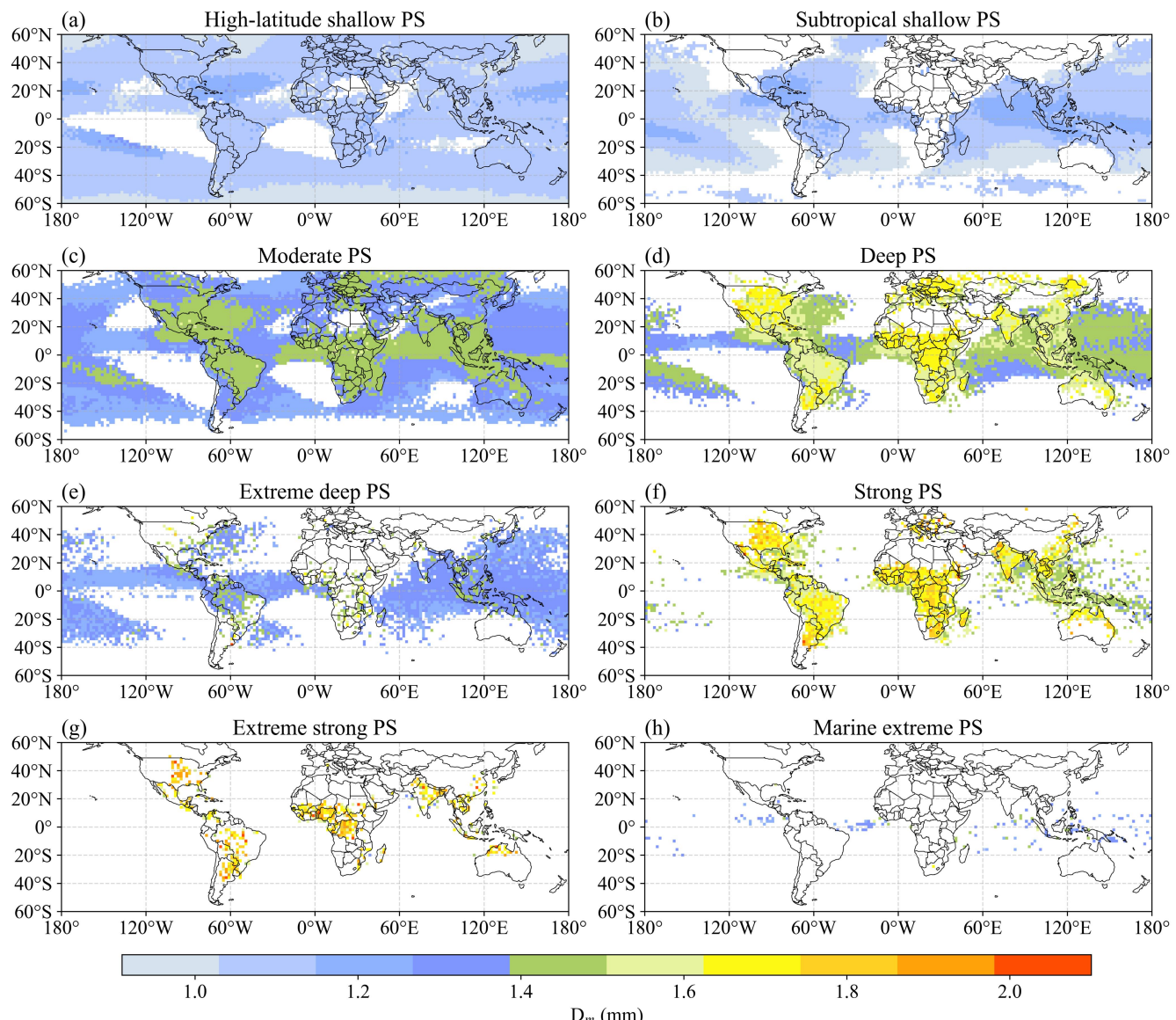
	high- latitude shallow PS	subtropical shallow PS	Moderate PS	deep PS	extreme deep PS	strong PS	extreme strong PS	marine extreme PS
Mean MAXHT20 (km)	3.40	3.29	7.03	11.89	12.67	15.39	17.21	12.85
Mean MAXHT30 (km)	2.63	2.67	5.11	8.65	8.52	13.68	16.31	9.18
Mean MAXHT40 (km)	0.00*	0.00*	3.44	5.53	5.71	8.64	12.32	6.04
Stratiform percentages (%)	88.63	9.46	54.38	53.22	69.90	57.42	53.02	66.83
Convective percentages (%)	5.85	89.95	42.83	44.52	28.16	39.91	44.06	31.56
Land percentages (%)	21.61	6.97	27.96	42.31	15.61	65.37	80.98	10.45
Ocean percentages (%)	78.39	93.03	72.04	57.69	84.39	34.63	19.02	89.55
Mean precipitation (mm h <sup>-1</sup> )	1.60	2.35	6.21	35.94	156.67	135.46	156.37	178.30
precipitation Standard deviation (mm h <sup>-1</sup> )	1.63	1.92	8.89	50.44	98.44	106.95	103.50	98.61
Number of samples	4,184,547	3,083,077	1,383,261	215,611	34,982	19,790	2,096	943
Mean precipitation area (km <sup>2</sup> )	610.57	239.23	2761.46	7009.37	37076.93	18485.91	22521.51	36044.11
>273.15 K frequency (%)	86.60	99.16	99.83	99.97	99.97	99.99	99.99	100.00
2.5 km Mean MAX-log10(N <sub>w</sub> ) [m <sup>-3</sup> mm <sup>-1</sup> ]	3.47	3.70	4.06	4.49	5.20	4.72	4.88	6.07
2.5 km Mean MAX-D <sub>m</sub> [mm]	1.03	1.17	2.26	2.82	2.71	3.04	3.11	2.61
2.5 km Mean log10(N <sub>w</sub> ) [m <sup>-3</sup> mm <sup>-1</sup> ]	3.23	3.45	3.36	3.39	3.83	3.36	3.35	4.45
2.5 km Mean D <sub>m</sub> [mm]	0.85	0.89	1.36	1.50	1.30	1.61	1.71	1.32

248 **3.2. Global distributions of microphysical features**

249 Fig. 2 and Fig. 3 show the global distributions of the microphysical parameters for the eight types of PSs. To avoid the  
250 influence of ground clutter, in each PS, the mean D<sub>m</sub> and N<sub>w</sub> values at 2.5 km above the ground surface were analyzed.  
251 Notably, there was a significant degree of spatial heterogeneity in each panel. The general conclusion is that continental PSs  
252 exhibit a higher D<sub>m</sub> than do oceanic PSs. Usually, continental rainfall is associated with high convective activity in which

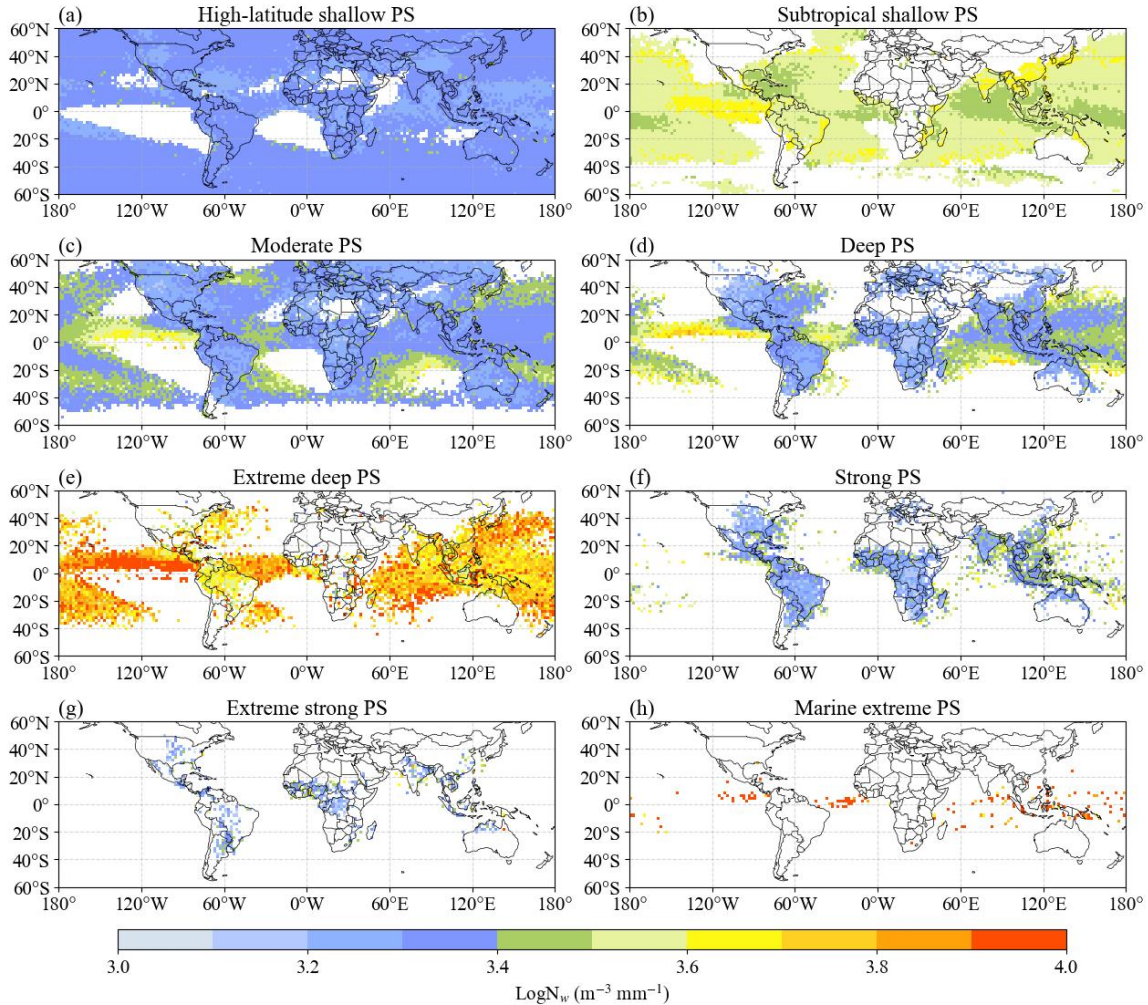


253 clouds produce large raindrops. Over land, small raindrops are lifted by updrafts, whereas large raindrops are formed from  
254 the melting of larger ice crystals. In contrast, oceanic rainfall is accompanied by the formation of weak updrafts and the  
255 development of a low melting layer, which impedes the formation of large raindrops and results in a high concentration of  
256 small raindrops (Saha et al., 2022; Seela et al., 2018). Moreover,  $D_m$  decreases with increasing latitude, a trend that is  
257 especially notable in high-latitude marine regions (refer to Fig. S2c in the Supplementary Material). Cha et al. (Cha and Yum,  
258 2021) noted that snow primarily comprises small particles (diameter  $< 1$  mm). In high-latitude shallow PS, snowfall may  
259 become more frequent from the middle to high latitudes, which can result in a decrease in  $D_m$ . Notably, the height and  
260 thickness of the melting layer may influence raindrop growth (Hu et al., 2024). With increasing latitude, the melting layer  
261 becomes thinner, thus reducing the conditions necessary for raindrop growth, which may lead to the formation of a larger  
262 number of small raindrops. In the oceanic regions within subtropical shallow PS, the higher sea surface temperature in the  
263 tropics is more conducive to convection formation and development. Moreover,  $D_m$  varies among the eight clusters in a  
264 specific region. For example, in the Amazon region, moderate PS exhibits a lower  $D_m$  than deep PS does.  
265 Similar to  $D_m$ , there is a distinct contrast in  $N_w$  between continents and oceans. Continental rainfall is usually associated with  
266 the cold rain mechanism, whereby raindrops grow as ice particles. In contrast, oceanic rainfall is associated with a warm rain  
267 regime, in which raindrops grow via a collision-agglomeration mechanism. Consequently,  $N_w$  over land is less than that over  
268 oceans (Suh et al., 2016). For the same PS,  $N_w$  is high in areas with small  $D_m$  values and conversely low in areas with large  
269  $D_m$  values. For example, in extreme deep PS, the  $D_m$  value over the eastern near-equatorial Pacific Ocean, which reaches  
270 approximately 1.18 mm, is smaller than that of the other oceanic regions. However,  $N_w$  is significantly greater than those in  
271 the other regions. In strong PS, the  $D_m$  values in near-equatorial Africa and the eastern United States are greater than those in  
272 other regions, but the  $N_w$  values are lower than those in other regions. It is possible that  $D_m$  and  $N_w$  may be negatively  
273 correlated for the same PS.



274

275 **Figure 2.** Spatial distributions of the mass-weighted mean diameter ( $D_m$ ) for the eight PS clusters at a height of 2.5 km.



276

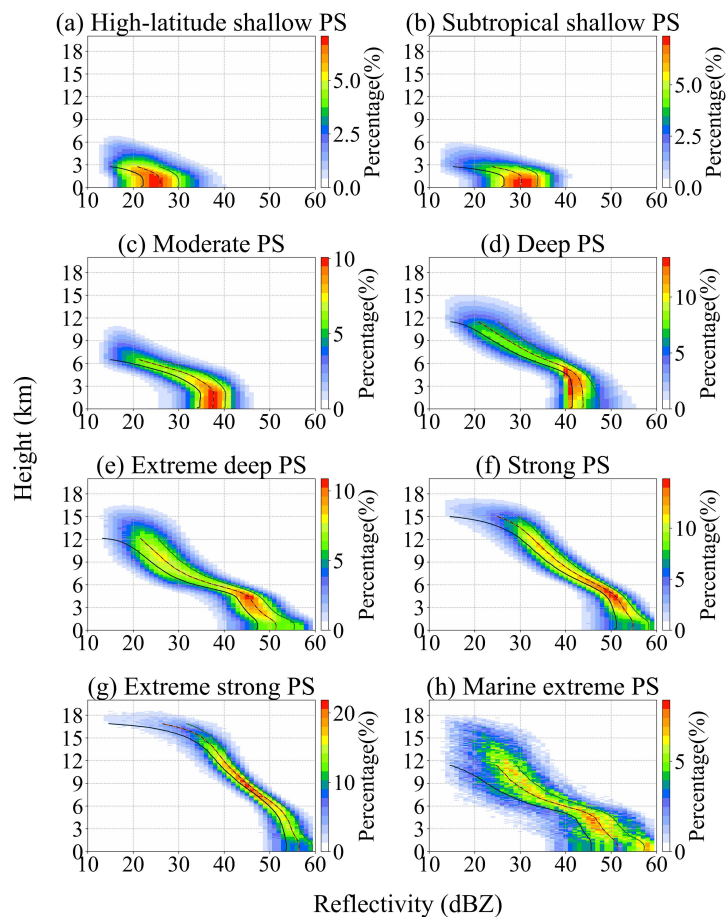
277 **Figure 3.** Similar to Fig. 2, but for  $\log_{10}(N_w)$ .

### 278 3.3. Vertical structure of the different PS types

279 The contoured frequency by altitude diagrams (CFADs) of  $D_m$ ,  $N_w$ , and the maximum radar reflectivity for the eight clusters  
280 are shown in Fig. 4/5/6. Figure 4 shows the CFAD of the maximum radar reflectivity profiles. The results revealed high echo  
281 tops for deep PS, extreme deep PS, strong PS, and extreme strong PS, and low echo tops for high-latitude shallow PS and  
282 subtropical shallow PS. Extreme strong PS attained an echo top height greater than 18 km, and it also exhibited the strongest  
283 convection at the middle level. Its geographic distribution was exclusively terrestrial, which is consistent with other studies  
284 concluding that deep convective cores occur mostly over land (Houze Jr. et al., 2015). Extreme deep PS and marine extreme  
285 PS exhibited sharper decreasing trends from 6–12 km than that in extreme strong PS. Therefore, extreme strong PS  
286 encompassed a greater amount of supercooled liquid droplets or large ice–water vapor condensates produced by strong

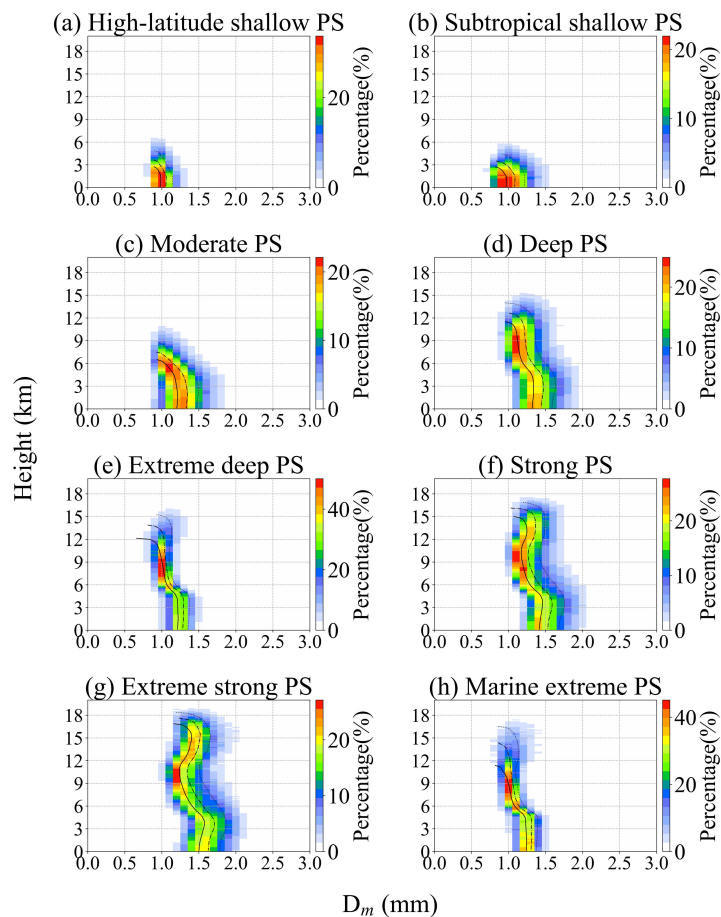


287 convective updrafts than that in extreme deep PS and marine extreme PS (Jiang, 2012). Owing to the lack of strong updrafts  
288 in extreme deep PS and marine extreme PS, the reflectivity rapidly decreased with height above the freezing level. Table 1  
289 indicates that the land proportion of extreme strong PS was much greater than that of extreme deep PS and marine extreme  
290 PS. Additionally, land indicates a dry adiabatic lapse rate, which results in greater buoyancy and allows for stronger updrafts  
291 to lift ice crystals higher into the atmosphere. As a result, the maximum radar reflectivity in the middle levels at high  
292 altitudes decreased more slowly in extreme strong PS. High-latitude shallow PS and subtropical shallow PS yielded low echo  
293 tops of less than 6 km, indicating low convective intensity. Therefore, subtropical shallow PS could be identified as being  
294 associated with isolated shallow convection over the ocean, especially the region dominated by the subtropical high.



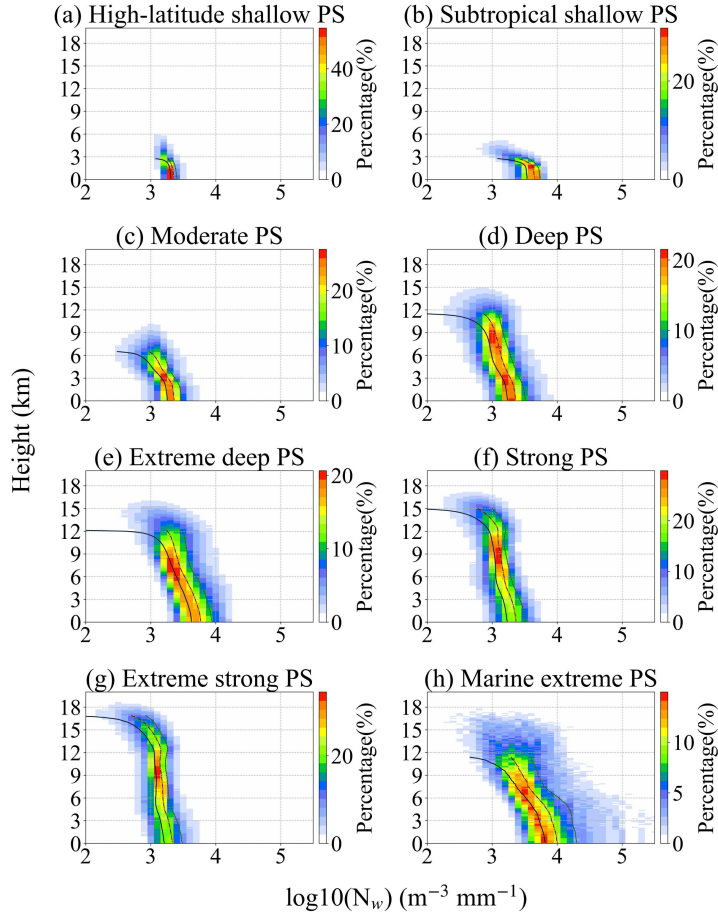


296 **Figure 4.** Contoured frequency by altitude diagrams (CFADs) of the maximum radar reflectivity for the eight distinct PS  
297 clusters. The solid lines indicate the 25th percentiles; the dashed-dotted lines indicate the 50th percentiles; the dotted lines  
298 indicate the 75th percentiles.



299

300 **Figure 5.** Similar to Fig. 4, but for  $D_m$ .



301

302 **Figure 6.** Similar to Fig. 4, but for  $\log_{10}(N_w)$ .

303 Figure 5 shows the CFAD of  $D_m$  for the eight types of PSs. Generally, deep convections (deep PS, extreme deep PS, strong  
304 PS, extreme strong PS, and marine extreme PS) produce different  $D_m$  values in the regions above and below approximately 5  
305 km. Moreover, strong PS and extreme strong PS exhibited wider distributions than those of extreme deep PS and marine  
306 extreme PS. For deep PS, strong PS, and extreme strong PS,  $D_m$  below 4.8 km did not change much or slightly increased  
307 along with height, but the value decreased between 4.8 and 6.9 km. In extreme strong PS, the vertical structure of  $D_m$  was  
308 more complex. Extreme strong PS exhibited three regimes according to the variations in  $D_m$ . The first regime was observed  
309 between 0 and 4.1 km, where  $D_m$  increases with altitude. This is consistent with other papers involving the use of ground-  
310 based radar observations and reporting that  $D_m$  of deep convective precipitation decreases with decreasing height near the  
311 surface (Marzuki et al., 2023). The observed decrease in  $D_m$  may be related to the continued breakdown of large isolated

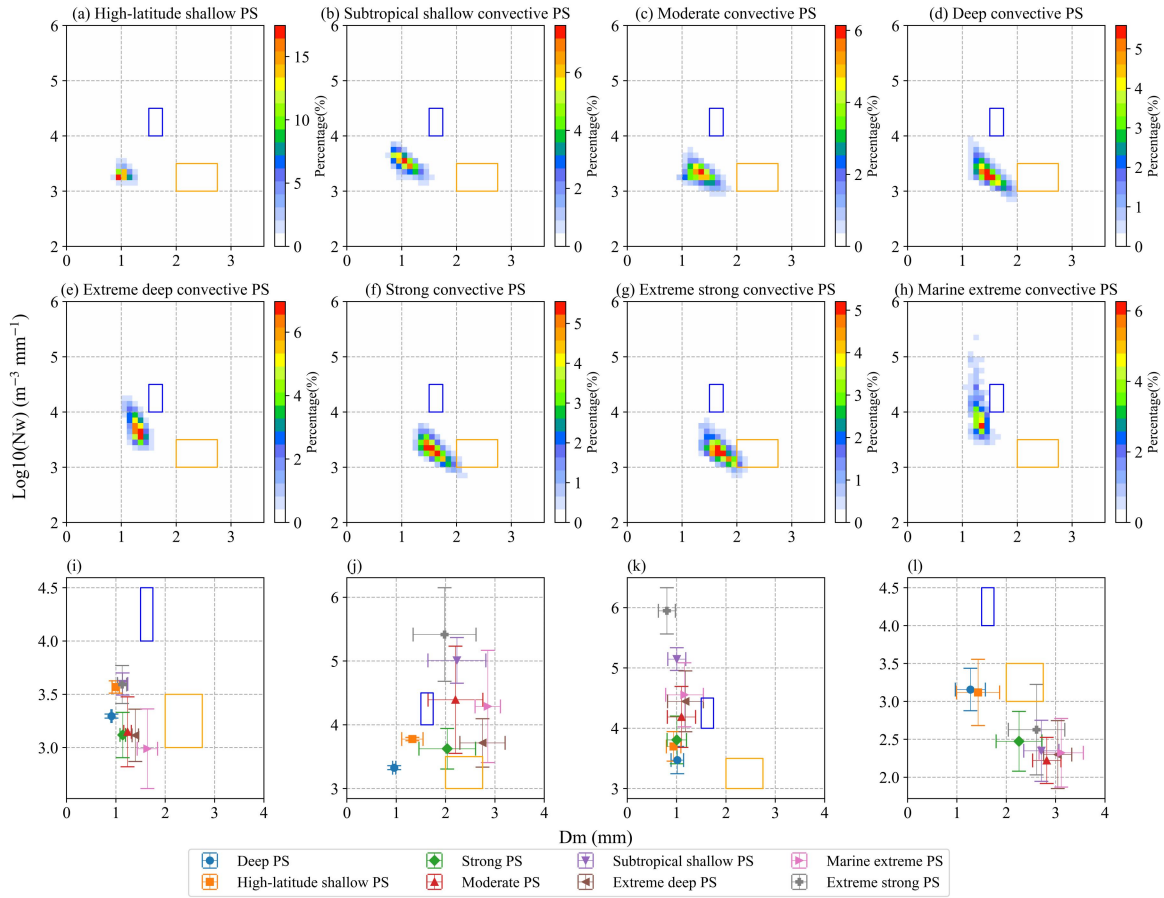


312 raindrops in the atmosphere. The second regime was observed above the freezing level, from 4.1 to 10 km, where  $D_m$   
313 decreases with altitude. In this regime, the updraft in deep convection was decreased (Uma and Rao, 2009). The decline in  
314 updraft decreased the size of the particles that can be retained in the cloud. Finally, the third regime was observed between  
315 10 and 18 km, where  $D_m$  increases with altitude and where strengthened updrafts are often observed (Becker and  
316 Hohenegger, 2021). Although both high-latitude shallow PS and subtropical shallow PS were shallow PSs, subtropical  
317 shallow PS had a wider distribution of  $D_m$  than high-latitude shallow PS. One possible reason is that in shallow oceanic  
318 convection, the breaking of large raindrops broadens the DSD.

319 Figure 6 shows the CFAD of  $\log_{10}(N_w)$  for the different types of PSs. In general,  $N_w$  decreases with increasing altitude. The  
320 distribution range of  $N_w$  for shallow PSs was relatively small. Moreover, the  $N_w$  distribution range of subtropical shallow PS  
321 was larger than that of high-latitude shallow PS. Among PSs with intense convection, PSs with a greater proportion of land  
322 coverage exhibited more concentrated  $N_w$  values, whereas PSs with a greater proportion of ocean coverage exhibited higher  
323  $N_w$  values. For example, the  $N_w$  values of strong PS and extreme strong PS were smaller and narrower than those of ocean-  
324 dominated deep PS, extreme deep PS and marine extreme PS. This finding is consistent with the conclusions of other studies  
325 (Kumar et al., 2024). One possible explanation is that the slower updrafts over ocean regions result in higher concentrations  
326 of smaller condensates at lower altitudes.

### 327 **3.4. DSD characteristics at a height of 2.5 km**

328 Figure 7a-h show the frequency distributions of the mean  $D_m$  and  $\log_{10}(N_w)$  values observed at 2.5 km above ground level.  
329 The mean  $D_m$  values for the eight types of PSs were 0.85, 0.89, 1.36, 1.50, 1.30, 1.61, 1.71, and 1.32 mm, and the  
330 corresponding  $\log_{10}(N_w)$  values were 3.23, 3.45, 3.36, 3.39, 3.83, 3.36, 3.35, and  $4.45 \text{ m}^{-3} \text{ mm}^{-1}$ , respectively, as detailed in  
331 Table 1. Generally, all the distributions shown in Fig. 7a-h greatly deviate from the parameters of continental convection and  
332 maritime convection defined by Bringi et al. (2003). One reason is that the mean values of  $D_m$  and  $N_w$  for one PS were  
333 considered here, whereas Bringi et al. (2003) separated the observation samples into stratiform and convection samples.  
334 Moreover, the DSDs observed by disdrometers are generally cumulative observations of a single storm at one fixed location  
335 and differ from the results for each PS in this study, which represent the instantaneous occurrence of a storm. With the most  
336 intense convection at the middle level, extreme strong PS was the closest to continental convection (Fig. 7d), whereas marine  
337 extreme PS was the closest to maritime convection (Fig. 7e). For most PSs,  $D_m$  and  $N_w$  were negatively correlated, with  
338 greater dispersion of  $D_m$  than that of  $N_w$ . Moreover, the shallow PSs, such as high-latitude shallow PS, exhibited lower  $D_m$   
339 and  $N_w$  values and more concentrated distributions than those of the deep PSs, such as those in deep PS.



340

341 **Figure 7.** (a-h) Two-dimensional frequency distributions of  $D_m$  and  $\log_{10}(N_w)$  at a height of 2.5 km, and (i-l) statistical  
342 values of  $\log_{10}(N_w)$  and  $D_m$  for each PS (the bar indicates one standard deviation). (i) Mean values of  $D_m$  and  $\log_{10}(N_w)$ , (j)  
343 MAX- $D_m$  and MAX- $\log_{10}(N_w)$ , (k) MAX- $\log_{10}(N_w)$  and  $D_m$  at its corresponding position, and (l) MAX- $D_m$  and  $\log_{10}(N_w)$   
344 at its corresponding position for each PS. (the blue and orange rectangles denote the maritime and continental convective  
345 clusters, respectively, in  $D_m$  and  $\log_{10}(N_w)$  space from Bringi et al. (2003)).

346 To further compare the mean  $D_m$  and  $N_w$  values of the different clusters, Figure 7i shows a summary of the mean  $D_m$  and  $N_w$   
347 values, with the standard deviation for each type of PS. Marine extreme PS showed a significant abnormal value of  $N_w$ ,  
348 whereas the  $N_w$  value of extreme deep PS slightly deviated from those of the other PS. However, if only three extremely  
349 deep PSs with the highest echo tops, as detailed in Table 1 (strong PS, extreme strong PS, and marine extreme PS), were  
350 considered, it could be concluded that the larger the  $D_m$  value is, the smaller the  $N_w$  value. Moreover, the other PSs exhibited  
351 very similar  $N_w$  values. These results might suggest that in deep convection, the DSD parameters at the near-surface level are  
352 related to convection intensity parameters. Ni et al. (2019) revealed that the dual-frequency ratio between the Ku and Ka



353 bands at 12 km was positively correlated with intensity parameters such as MAXHT20/30, partly because stronger updrafts  
354 could hold larger ice particles in clouds. However, in shallow convection systems such as those in high-latitude shallow PS  
355 and subtropical shallow PS, the relationship did not hold, which rendered the relationship between microphysical parameters  
356 and convection parameters complex.

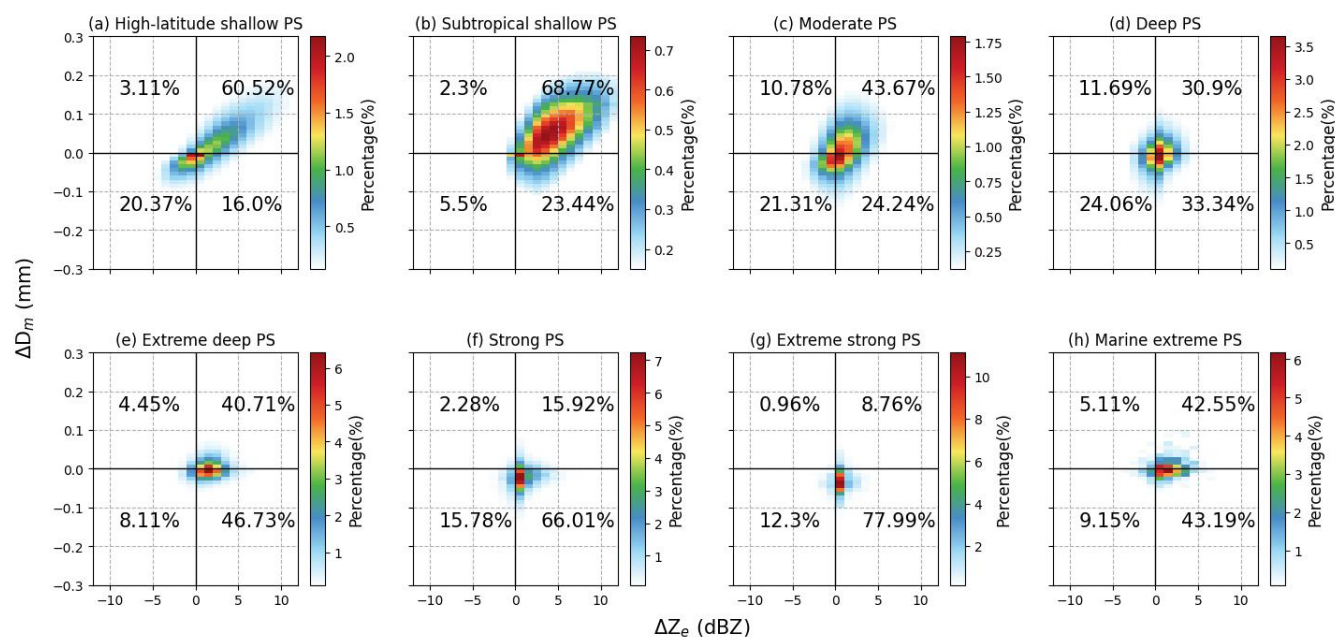
357 Note that although the mean  $D_m$  and  $N_w$  values represent the overall features of DSDs in one PS, they do not capture the  
358 variety of DSDs in each PS. For example, the DSD might differ between convective and stratiform regions, where the  $N_w$ –  
359  $D_m$  relationships might vary. To comprehensively demonstrate the microphysical features of PSs, Figure 7j shows the mean  
360 MAX- $D_m$  and MAX- $N_w$  values of each PS at 2.5 km above ground level. For extreme PS (extreme deep PS, strong PS,  
361 extreme strong PS, and marine extreme PS), a negative correlation was found between MAX- $D_m$  and MAX- $N_w$ , similar to  
362 the mean  $D_m$  and  $N_w$  values shown in Fig. 7h. However, for the non-extreme PS, MAX- $D_m$  and MAX- $N_w$  exhibited positive  
363 correlations. A similar relationship is also shown in Fig. 7k, which suggests a relationship between MAX- $N_w$  and the  
364 corresponding  $D_m$  value in the MAX- $N_w$  pixels of each PS. Nevertheless, as shown in Fig. 7k, the  $D_m$  values of all eight  
365 types of PSs were very close. Nevertheless, it could be also found that in the non-extreme PS the  $D_m$  increases with MAX- $N_w$ ,  
366 while in the extreme PS, the  $D_m$  decreases with MAX- $N_w$ . Figure 7l shows the relationship between MAX- $D_m$  and the  
367 corresponding  $N_w$  value in the MAX- $D_m$  pixels of each PS. Interestingly, for all eight types of PSs, MAX- $D_m$  and  $N_w$  showed  
368 significantly negative correlations. Note that MAX- $D_m$  and MAX- $N_w$  in Fig. 7j are the maximum values for one PS and  
369 usually do not occur in the same pixel. Figure 7k–l show the  $N_w$ – $D_m$  relationship observed at the same location. Overall, the  
370 conclusions generally indicated that deep PSs yield larger MAX- $N_w$  or MAX- $D_m$  values than shallow convection PSs do.  
371 Overall, extreme PS exhibited negative correlations between  $N_w$  and  $D_m$ , whereas non-extreme PS demonstrated positive  
372 correlations.

373 Ryu et al. (2021) analyzed DSDs during three types of heavy rainfall events with different rain intensities. They also  
374 reported that  $D_m$  increases with increasing rainfall intensity, whereas  $N_w$  decreases with increasing rainfall intensity. In this  
375 study, we saw a positive relationship between the increase in  $D_m$  and MAXHT20 in extreme PS. However, extreme strong  
376 PS attained the highest MAXHT20 value, but its precipitation rate was lower than that of extreme deep PS and marine  
377 extreme PS. These results suggest a complex relationship between the microphysical parameters and convection features,  
378 especially in deep and intense convection systems. Notably, in extreme convection, with strong convection at the top of the  
379 storm, attenuation becomes notable at low storm levels, which might influence the retrieval of microphysical parameters. To  
380 assess the impact of attenuation on the  $D_m$ – $N_w$  relationship, ground-based observations of microphysical properties from  
381 disdrometers are needed. Finally, we considered the PS as a whole and did not account for the variations in the  $D_m$  and  $N_w$   
382 values of each PS. The microphysical characteristics varied among different pixels. The mean or maximum values of  $D_m$  and  
383  $N_w$  only reflect part of the total process. Therefore, analyses on the basis of pixel-level observations would improve this  
384 work.

385 To gain further insight into the primary microphysical processes associated with the various PS, we employed an  
386 investigative approach analogous to that utilized by Kumjian and Prat (2014). To prevent the influence of ground-based



387 clutter,  $\Delta Z_e$  and  $\Delta D_m$  values were calculated as the difference between  $Z_e$  and  $D_m$  at 2 and 3 km above the ground.  
388 Specifically,  $\Delta Z_e = Z_e^{2\text{km}} - Z_e^{3\text{km}}$  and  $\Delta D_m = D_m^{2\text{km}} - D_m^{3\text{km}}$  are calculated. Fig. 8 shows the frequency pattern of  $\Delta Z_e$  versus  
389  $\Delta D_m$  for the eight types of PSs. An increase (decrease) in  $Z_e$  and  $D_m$  indicates that coalescence (breakup) processes dominate.  
390 Balanced breakup and coalescence processes result in an increase in  $Z_e$  but a decrease in  $D_m$ . In contrast, a decrease in  $Z_e$  and  
391 an increase in  $D_m$  are due to predominate evaporation or size sorting processes (Wen et al., 2023).  
392 The microphysical processes of the different types of PSs were significantly distinct. Notably, the microphysical processes  
393 were dominated by coalescence in the two types of shallow PS (Fig. 8a-b). Previous studies have demonstrated that high-  
394 latitude shallow PS are more likely to experience the condensation of rain droplets into snow due to the low temperatures in  
395 these regions. (Thompson et al., 2015). Meanwhile, the coalescence process plays an important role in tropical oceanic  
396 shallow convective precipitation (subtropical shallow PS) as demonstrated by Li et al. (2024). Balanced breakup and  
397 coalescence processes in the microphysical processes of extreme PS accounted for more than 40% of the total microphysical  
398 processes, significantly exceeding other three types of microphysical processes. The microphysical processes may reach an  
399 equilibrium state under high rainfall rates, in which the coalescence and breakup of raindrops are nearly balanced. Extreme  
400 deep PS and marine extreme PS encompassed a higher percentage of coalescence processes than strong PS and extreme  
401 strong PS did, whereas strong PS and extreme strong PS encompassed a higher percentage of breakup processes.



402

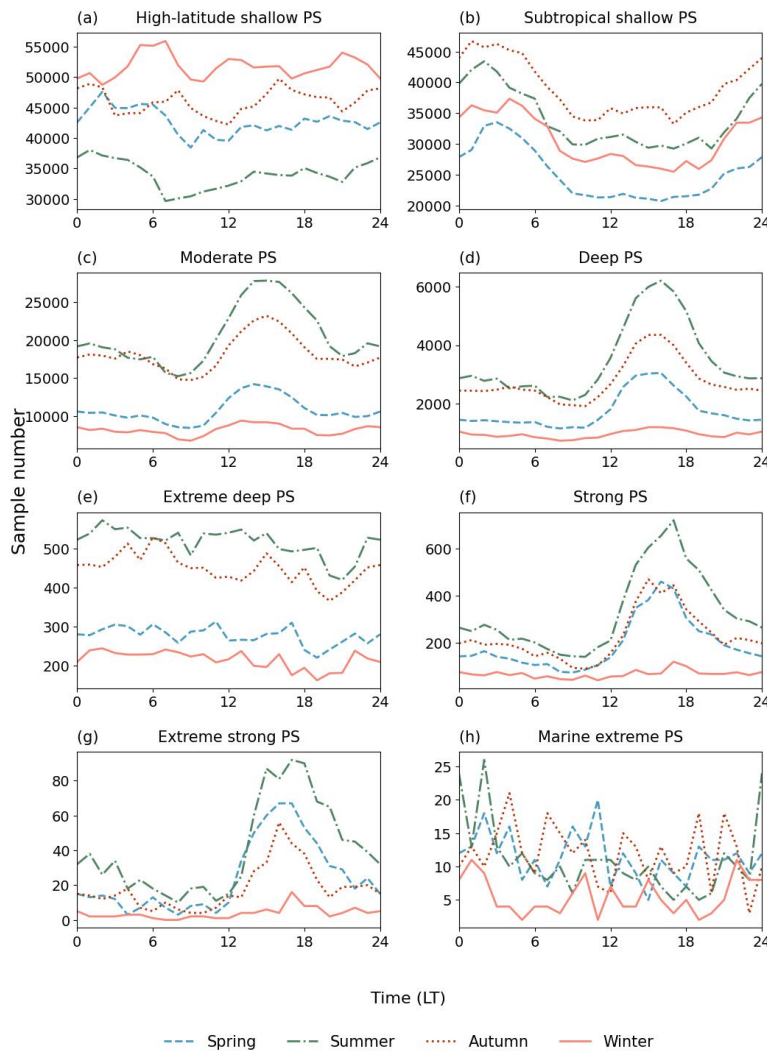
403 **Figure 8.** Frequency pattern of  $\Delta Z_e$  versus  $\Delta D_m$  between 2 and 3 km for the eight PS clusters.



404 **3.5. Seasonal and diurnal cycles**

405 In this study, seasons were categorized by fixed calendar months. The Northern Hemisphere seasons were defined as spring  
406 (March–May), summer (June–August), autumn (September–November), and winter (December–February). Conversely, the  
407 Southern Hemisphere seasons followed the opposite pattern: spring (September–November), summer (December–February),  
408 autumn (March–May), and winter (June–August). Based on this classification, the subsequent analysis examines seasonal  
409 and diurnal variations in PS frequency and microphysical parameters. Figure 9 shows the cycles of PS occurrence. Overall,  
410 the seasonal and diurnal cycles differed among the eight types of PSs. Moderate PS, deep PS, strong PS, and extreme strong  
411 PS exhibited cycles like those of continental convection systems, with peaks in the afternoon and in summer. Dominated by  
412 tropical shallow convection over the ocean (Fig. 1), subtropical shallow PS occurred mostly between 0 and 5 a.m. and was  
413 more frequent during the autumn season than during the other seasons, with the lowest occurrence during the spring season.  
414 The other types of PS (high-latitude shallow PS, extreme deep PS, and marine extreme PS) did not show obvious diurnal  
415 cycles, except that high-latitude shallow PS indicated a low peak at approximately 6 am in winter and a valley before noon in  
416 summer. High-latitude shallow PS occurred infrequently in winter. Extreme deep PS occurred more frequently in summer  
417 and autumn, with fewer occurrences in winter. Note that marine extreme PS did not demonstrate obvious seasonal  
418 discrepancies, but shown a peak at night in the summer. Specifically, strong PS and extreme strong PS with a higher  
419 proportion over land exhibit a peak occurrence around 3 p.m. in the afternoon, while extreme deep PS and marine extreme  
420 PS with a higher proportion over the ocean shows no distinct peak, with its frequency distributed relatively evenly  
421 throughout the day. This difference reflects the land-ocean contrast in extreme PS, which is consistent with findings from  
422 other related studies (Wang and Tang, 2020).

423



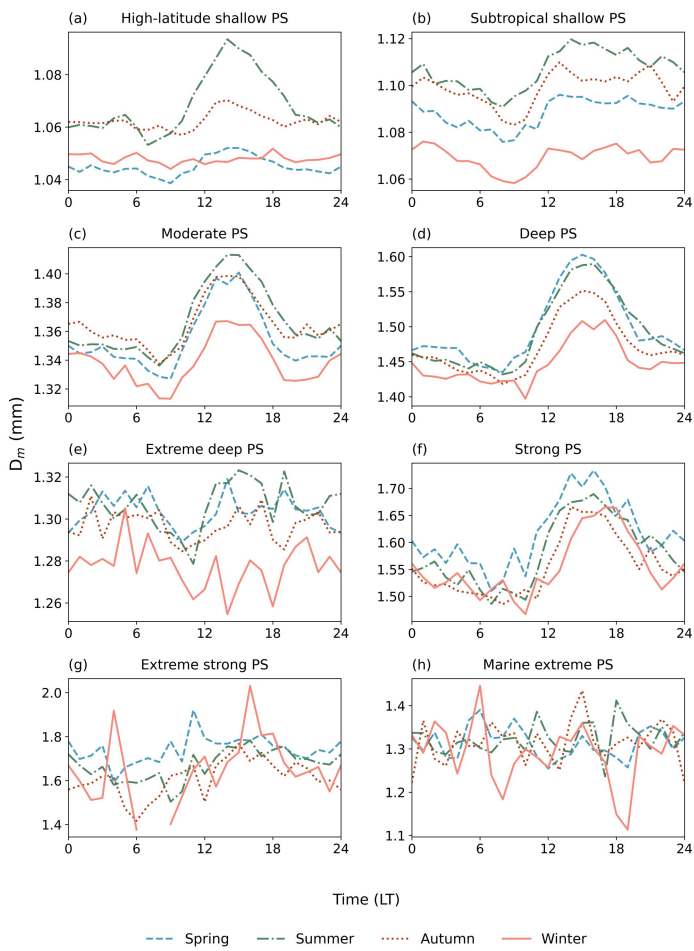
424

425 **Figure 9.** Diurnal variations in the sample sizes of the eight distinct PS clusters across the four seasons.

426 Figures 10 and 11 show the seasonal and diurnal cycles of  $D_m$  and  $N_w$ , respectively. The diurnal cycles of  $D_m$  were similar  
427 with those of PS occurrence to some extent. For example, in moderate PS, deep PS and strong PS, both the occurrence and  
428  $D_m$  have peaks in the around 15 pm. One connection between these two parameters is that environments that favor storm  
429 occurrence could also facilitate the development of stronger updrafts, which could promote the formation of large particles in  
430 clouds. Nevertheless, discrepancies are obvious between the cycles of occurrence and  $D_m$ . For example, the  $D_m$  in the  
431 extreme strong PS did not show obvious diurnal variations. The high-latitude shallow PS shows a peak in the summer (Fig.  
432 10a), which is not found in the diurnal cycle of occurrence (Fig. 9a). In subtropical shallow PS, the diurnal cycle of  $D_m$  (Fig.  
433 10b) was the opposite to that of PS occurrence (Fig. 9b). The diurnal cycles of  $N_w$  were basically different with those of  $D_m$   
434 and occurrence. In subtropical shallow PS, moderate PS, deep PS, and strong PS, the  $N_w$  peaked in the morning.

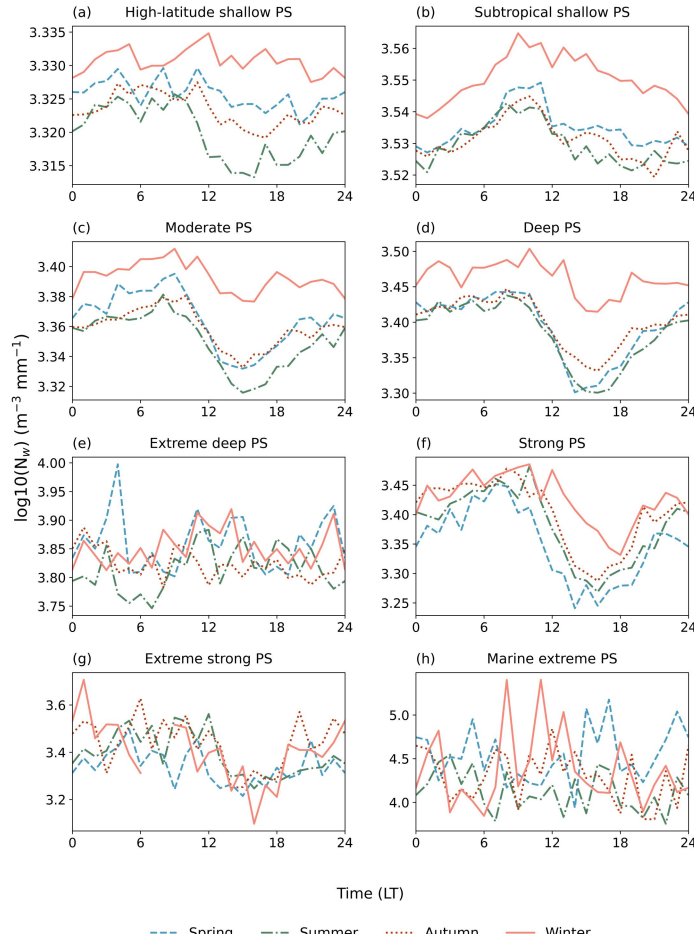


435 Nevertheless, the diurnal cycles of subtropical shallow PS, moderate PS, and deep PS also differed. For example,  $N_w$  of  
436 subtropical shallow PS at night was low, whereas  $N_w$  of shallow convective PS and moderate PS at night was very close to  
437 its peak. Extreme deep PS and marine extreme PS did not exhibit obvious diurnal cycles of  $N_w$ . The extreme strong PS  
438 shown low values of  $N_w$  in the afternoon and little variations at night. For high-latitude shallow PS, diurnal variation is not  
439 clear except in the summer when the  $N_w$  in the afternoon is the lowest.



440

441 **Figure 10.** Similar to Fig. 9 but for mean  $D_m$  value.



442

443 **Figure 11.** Similar to Fig. 9 but for the mean  $\log_{10}(N_w)$  value.

444 Similar to the diurnal cycles, the annual cycles of  $D_m$  and  $N_w$  were opposite in subtropical shallow PS, moderate PS, and  
445 deep PS, of which  $D_m$  was the lowest and  $N_w$  was the largest in winter. Nevertheless, there were also differences in the  
446 annual cycles of the three types of PSs. For example, in subtropical shallow PS,  $D_m$  was the largest in summer, followed by  
447 autumn and spring, whereas the  $N_w$  values during the three seasons were very close. Among the extreme PS,  $N_w$  and  $D_m$  did  
448 not exhibit obvious annual cycles. For high-latitude shallow PS, the highest  $D_m$  value occurs in summer and the  $D_m$  in winter  
449 and spring were comparable. However, the annual cycle of  $N_w$  attained the largest value in winter and the lowest value in  
450 summer.



#### 451 4. Conclusions

452 In this study, GPM DPR data were used to objectively classify global PS and analyze the microphysical characteristics of the  
453 different types of PS. The main conclusions are as follows:

454 1). By conducting an objective classification of global PSs via key parameters such as the convective intensity, radar  
455 reflectivity, and DSD parameters, eight distinct types of PSs were identified. These systems were classified on the basis of  
456 their unique microphysical and convection properties, providing a detailed understanding of the different precipitation  
457 processes worldwide. The eight types of PSs identified are as four types of regular/non-extreme PS (high-latitude shallow PS,  
458 subtropical shallow PS, moderate PS, deep PS) and four types of extreme PS (extreme deep PS, strong PS, extreme strong  
459 PS, marine extreme PS).

460 2). MAXHT20 is generally correlated with the precipitation rate, but this relationship is not clear for extreme PS. The  
461 relationship between MAXHT20 and  $D_m$  does not follow a simple linear pattern. For extreme PS, MAXHT20 is positively  
462 related to  $D_m$  at 2.5 km above the ground surface. This may reflect the relationship between higher cloud tops and greater  
463 liquid water contents in strongly convective PSs. However, for non-extreme PS, the relationship between MAXHT20 and  $D_m$   
464 is more complex and may be influenced by variations in the physical processes of the different PS.

465 3). For the same type of PS,  $D_m$  over land is greater than that over the ocean. Additionally,  $D_m$  exhibits latitudinal variability,  
466 particularly in high-latitude shallow PS, where  $D_m$  decreases with increasing latitude. Additionally, continental rainfall is  
467 associated with lower  $N_w$  values due to the cold rain mechanism, whereas oceanic rainfall is associated with higher  $N_w$   
468 values resulting from a warm rain regime. Shallow PS generally exhibit narrow distributions of both  $D_m$  and  $N_w$ , particularly  
469 in high-latitude shallow PS. Among the strong PS, PS with a higher land proportion exhibit more concentrated  $N_w$  values,  
470 whereas those with a greater ocean proportion exhibit larger  $N_w$  values. However, the distribution of  $D_m$  is the opposite: PS  
471 with a higher ocean proportion exhibit more concentrated  $D_m$  values than land-dominated PSs do.

472 4). The different PS exhibit distinct microphysical processes. In shallow convective PS, such as subtropical shallow PS and  
473 high-latitude shallow PS, coalescence processes largely shape the microphysical characteristics, indicating the aggregation of  
474 small raindrops in these PS. In contrast, extreme PSs are characterized by balanced breakup and coalescence processes,  
475 highlighting a more complex interaction between raindrop formation and breakup. These results emphasize the varying  
476 mechanisms that govern microphysical behavior across the different types of PSs. PS types with high precipitation rates are  
477 dominated primarily by balanced breakup and coalescence processes, whereas shallow PSs are characterized mainly by  
478 coalescence.

479 5). The seasonal and diurnal cycles of PSs and their microphysical parameters vary significantly, with distinct patterns  
480 observed in different clusters: clusters dominated by continental convection indicate peaks in the afternoon and summer,  
481 whereas tropical and high-latitude systems exhibit unique seasonal and diurnal cycles, often with opposite trends between  
482  $D_m$  and  $N_w$ .



483 Classifying PS is essential for increasing the understanding of the microphysical processes that govern cloud development  
484 and precipitation formation across various climatic regimes. This classification enables the identification of specific  
485 mechanisms that influence rainfall characteristics, such as droplet formation, growth, and distribution, which are vital for  
486 accurate weather predictions and climate modeling. This study revealed the global distribution characteristics of different  
487 types of PS and elucidated the variations in microphysical properties across regions with distinct climatic and geographic  
488 conditions.

489 In this study, each PS was treated as integrated entity, without considering the variations in  $D_m$  and  $N_w$  within each system.  
490 Microphysical properties can vary significantly at the pixel level, and relying solely on average or maximum  $D_m$  and  $N_w$   
491 values captures only part of the overall process. Future work should focus on analyzing pixel-level observations to better  
492 understand the characteristics of microphysical parameters within PS. Furthermore, investigating the relationships between  
493 microphysical parameters and convective parameters will be a key focus of future research. By analyzing the interactions  
494 between these parameters, it is possible to reveal the influences of microphysical characteristics on convective intensity and  
495 precipitation patterns, providing a more detailed perspective for accurately predicting and understanding precipitation  
496 phenomena.

497 **Data Availability.** The GPM-DPR (version 07A) data from the NASA/Goddard Space Flight Center are available at  
498 [https://disc.gsfc.nasa.gov/datasets/GPM\\_2A-DPR\\_07/summary](https://disc.gsfc.nasa.gov/datasets/GPM_2A-DPR_07/summary). All statistics and visualization are operated with Anaconda  
499 Individual Edition Python version 3.8.3 (Free Download | Anaconda, accessed on 10 April 2022).

500 **Author contributions.** XZ and XN conceptualised and planned the research study. XZ conducted the satellite data analysis  
501 with support from XN and drafted the initial manuscript. XN and JZ reviewed and revised the manuscript to refine its  
502 content.

503 **Competing interests.** The contact author has declared that none of the authors has any competing interests.

504 **Financial support.** This study is supported by the National Natural Science Foundation of China (42105005), Fundamental  
505 Research Funds for the Central Universities (SWU-KT22007), and General Program of Chongqing Natural Science  
506 Foundation (2022NSCQ-MSX3145).

## 507 References

508 Arulraj, M. and Barros, A. P.: Automatic detection and classification of low-level orographic precipitation processes from  
509 space-borne radars using machine learning, *Remote Sens. Environ.*, 257, 112355, <https://doi.org/10.1016/j.rse.2021.112355>,  
510 2021.

511 Awaka, J., Le, M., Brodzik, S., Kubota, T., Masaki, T., Chandrasekar, V., and Iguchi, T.: Development of precipitation type  
512 classification algorithms for a full scan mode of GPM dual-frequency precipitation radar, *J. Meteorol. Soc. Japan. Ser. II*, 99,  
513 1253–1270, <https://doi.org/10.2151/jmsj.2021-061>, 2021.

514 Ay, M., Özbakır, L., Kulluk, S., Gülməz, B., Öztürk, G., and Özer, S.: FC-Kmeans: Fixed-centered K-means algorithm,  
515 *Expert Syst. Appl.*, 211, 118656, <https://doi.org/10.1016/j.eswa.2022.118656>, 2023.



516 Becker, T. and Hohenegger, C.: Entrainment and its dependency on environmental conditions and convective organization in  
517 convection-permitting simulations, *Mon. Weather Rev.*, 149, 537–550, <https://doi.org/10.1175/MWR-D-20-0229.1>, 2021.

518 Bringi, V. N., Chandrasekar, V., Hubbert, J., Gorgucci, E., Randeu, W. L., and Schoenhuber, M.: Raindrop size distribution  
519 in different climatic regimes from disdrometer and dual-polarized radar analysis, *J. Atmos. Sci.*, 60, 354–365,  
520 [https://doi.org/10.1175/1520-0469\(2003\)060<0354:RSDIDC>2.0.CO;2](https://doi.org/10.1175/1520-0469(2003)060<0354:RSDIDC>2.0.CO;2), 2003.

521 Cha, J. W. and Yum, S. S.: Characteristics of precipitation particles measured by PARASIVEL disdrometer at a mountain and  
522 a coastal site in Korea, *Asia-Pac. J. Atmos. Sci.*, 57, 261–276, <https://doi.org/10.1007/s13143-020-00190-6>, 2021.

523 Chen, B. and Liu, C.: Warm organized rain systems over the tropical eastern Pacific, *J. Clim.*, 29, 3403–3422,  
524 <https://doi.org/10.1175/JCLI-D-15-0177.1>, 2016.

525 Chen, B., Hu, W., and Pu, J.: Characteristics of the raindrop size distribution for freezing precipitation observed in southern  
526 China, *J. Geophys. Res. Atmos.*, 116, <https://doi.org/10.1029/2010JD015305>, 2011.

527 Chudler, K., Rutledge, S. A., and Dolan, B.: Unique radar observations of large raindrops in tropical warm rain during  
528 PISTON, *Mon. Weather Rev.*, 150, 2719–2736, <https://doi.org/10.1175/MWR-D-21-0298.1>, 2022.

529 D'Adderio, L. P., Vulpiani, G., Porcù, F., Tokay, A., and Meneghini, R.: Comparison of GPM Core Observatory and  
530 Ground-Based Radar Retrieval of Mass-Weighted Mean Raindrop Diameter at Midlatitude, *J. Hydrometeor.*, 19, 1583–1598,  
531 <https://doi.org/10.1175/JHM-D-18-0002.1>, 2018.

532 Dai, Q., Zhu, J., Zhang, S., Zhu, S., Han, D., and Lv, G.: Estimation of rainfall erosivity based on WRF-derived raindrop size  
533 distributions, *Hydrol. Earth Syst. Sci.*, 24, 5407–5422, <https://doi.org/10.5194/hess-24-5407-2020>, 2020.

534 Das, S., Wang, Y., Gong, J., Ding, L., Munchak, S. J., Wang, C., Wu, D. L., Liao, L., Olson, W. S., and Barahona, D. O.: A  
535 comprehensive machine learning study to classify precipitation type over land from Global Precipitation Measurement  
536 Microwave Imager (GPM-GMI) measurements, *Remote Sens.*, 14, 3631, <https://doi.org/10.3390/rs14153631>, 2022.

537 Dolan, B., Fuchs, B., Rutledge, S. A., Barnes, E. A., and Thompson, E. J.: Primary modes of global drop size distributions, *J.*  
538 *Atmos. Sci.*, 75, 1453–1476, <https://doi.org/10.1175/JAS-D-17-0242.1>, 2018.

539 El Khattabi, M.-Z., El Jai, M., Lahmadi, Y., Oughdir, L., and Rahhali, M.: Understanding the interplay between metrics,  
540 normalization forms, and data distribution in k-means clustering: A comparative simulation study, *Arab. J. Sci. Eng.*, 49,  
541 2987–3007, <https://doi.org/10.1007/s13369-023-07741-9>, 2024.

542 Festa, D., Novellino, A., Hussain, E., Bateson, L., Casagli, N., Confuorto, P., Del Soldato, M., and Raspini, F.: Unsupervised  
543 detection of InSAR time series patterns based on PCA and K-means clustering, *Int. J. Appl. Earth Obs. Geoinf.*, 118, 103276,  
544 <https://doi.org/10.1016/j.jag.2023.103276>, 2023.

545 Gang, A. and Bajwa, W. U.: FAST-PCA: A fast and exact algorithm for distributed principal component analysis, *IEEE*  
546 *Trans. Signal Process.*, 70, 6080–6095, <https://doi.org/10.1109/TSP.2022.3229635>, 2022.

547 Gatlin, P. N., Petersen, W. A., Pippitt, J. L., Berendes, T. A., Wolff, D. B., and Tokay, A.: The GPM validation network and  
548 evaluation of satellite-based retrievals of the rain drop size distribution, *Atmosphere*, 11, 1010,  
549 <https://doi.org/10.3390/atmos11091010>, 2020.

550 Hamada, A., Takayabu, Y. N., Liu, C., and Zipser, E. J.: Weak linkage between the heaviest rainfall and tallest storms, *Nat.*  
551 *Commun.*, 6, 6213, <https://doi.org/10.1038/ncomms7213>, 2015.



552 Hou, A. Y., Kakar, R. K., Neeck, S., Azarbarzin, A. A., Kummerow, C. D., Kojima, M., Oki, R., Nakamura, K., and Iguchi,  
553 T.: The global precipitation measurement mission, *Bull. Amer. Meteor. Soc.*, 95, 701–722, <https://doi.org/10.1175/BAMS-D-13-00164.1>, 2014.

555 Houze Jr., R. A., Rasmussen, K. L., Zuluaga, M. D., and Brodzik, S. R.: The variable nature of convection in the tropics and  
556 subtropics: A legacy of 16 years of the Tropical Rainfall Measuring Mission satellite, *Rev. Geophys.*, 53, 994–1021,  
557 <https://doi.org/10.1002/2015RG000488>, 2015.

558 Hu, X., Ai, W., Qiao, J., and Yan, W.: Insight into global climatology of melting layer: latitudinal dependence and  
559 orographic relief, *Theor. Appl. Climatol.*, 155, 4863–4873, <https://doi.org/10.1007/s00704-024-04926-6>, 2024.

560 Iguchi, T., Kozu, T., Meneghini, R., Awaka, J., and Okamoto, K.: Rain-Profiling algorithm for the TRMM precipitation  
561 radar, *J. Appl. Meteor. Climatol.*, 39, 2038–2052, [https://doi.org/10.1175/1520-0450\(2001\)040<2038:RPAFTT>2.0.CO;2](https://doi.org/10.1175/1520-0450(2001)040<2038:RPAFTT>2.0.CO;2),  
562 2000.

563 Jain, A. K.: Data clustering: 50 years beyond K-means, *Pattern Recogn. Lett.*, 31, 651–666,  
564 <https://doi.org/10.1016/j.patrec.2009.09.011>, 2010.

565 Jiang, H.: The relationship between tropical cyclone intensity change and the strength of inner-core convection, *Mon. Weather Rev.*, 140, 1164–1176, <https://doi.org/10.1175/MWR-D-11-00134.1>, 2012.

567 Jolliffe, I. T. and Cadima, J.: Principal component analysis: a review and recent developments, *Phil. Trans. R. Soc. A*, 374,  
568 20150202, <https://doi.org/10.1098/rsta.2015.0202>, 2016.

569 Kumar, K. S., Das, S. K., Deshpande, S. M., Deshpande, M., and Pandithurai, G.: Regional variability of precipitation  
570 characteristics in tropical cyclones over the North Indian Ocean from GPM-DPR measurements, *Atmos. Res.*, 283, 106568,  
571 <https://doi.org/10.1016/j.atmosres.2022.106568>, 2023.

572 Kumar, S., Flores-Rojas, J. L., Moya-Álvarez, A. S., Martínez-Castro, D., and Silva, Y.: Hydrometeors distribution in  
573 intense precipitating cloud cells over the earth's during two rainfall seasons, *J. Indian Soc. Remote Sens.*, 52, 95–111,  
574 <https://doi.org/10.1007/s12524-023-01805-x>, 2024.

575 Kumjian, M. R. and Prat, O. P.: The impact of raindrop collisional processes on the polarimetric radar variables, *J. Atmos. Sci.*, 71, 3052–3067, <https://doi.org/10.1175/JAS-D-13-0357.1>, 2014.

577 Lerber, A. von, Moisseev, D., Marks, D. A., Petersen, W., Harri, A.-M., and Chandrasekar, V.: Validation of GMI snowfall  
578 observations by using a combination of weather radar and surface measurements, *J. Appl. Meteorol. Climatol.*, 57, 797–820,  
579 <https://doi.org/10.1175/JAMC-D-17-0176.1>, 2018.

580 Li, D., Qi, Y., and Li, H.: Statistical characteristics of convective and stratiform precipitation during the rainy season over  
581 South China based on GPM-DPR observations, *Atmos. Res.*, 301, 107267, <https://doi.org/10.1016/j.atmosres.2024.107267>,  
582 2024.

583 Liu, C.: Rainfall contributions from precipitation systems with different sizes, convective intensities, and durations over the  
584 Tropics and Subtropics, *J. Hydrometeorol.*, 12, 394–412, <https://doi.org/10.1175/2010JHM1320.1>, 2011.

585 Liu, C. and Zipser, E. J.: The global distribution of largest, deepest, and most intense precipitation systems, *Geophys. Res. Lett.*, 42, 3591–3595, <https://doi.org/10.1002/2015GL063776>, 2015.



587 Liu, C., Zipser, E. J., Cecil, D. J., Nesbitt, S. W., and Sherwood, S.: A cloud and precipitation feature database from nine  
588 years of TRMM observations, *J. Appl. Meteorol. Climatol.*, 47, 2712–2728, <https://doi.org/10.1175/2008JAMC1890.1>, 2008.

589 Liu, N., Liu, C., and Hayden, L.: Climatology and detection of overshooting convection from 4 years of GPM precipitation  
590 radar and passive microwave observations, *J. Geophys. Res. Atmos.*, 125, e2019JD032003,  
591 <https://doi.org/10.1029/2019JD032003>, 2020.

592 Marra, A. C., Porcù, F., Baldini, L., Petracca, M., Casella, D., Dietrich, S., Mugnai, A., Sanò, P., Vulpiani, G., and  
593 Panegrossi, G.: Observational analysis of an exceptionally intense hailstorm over the Mediterranean area: Role of the GPM  
594 Core Observatory, *Atmos. Res.*, 192, 72–90, <https://doi.org/10.1016/j.atmosres.2017.03.019>, 2017.

595 Marukatat, S.: Tutorial on PCA and approximate PCA and approximate kernel PCA, *Artif. Intell. Rev.*, 56, 5445–5477,  
596 <https://doi.org/10.1007/s10462-022-10297-z>, 2023.

597 Marzuki, M., Ramadhan, R., Yusnaini, H., Renggono, F., Vonnisa, M., and Hashiguchi, H.: Comparison of vertical profile of  
598 raindrop size distribution from micro rain radar with global precipitation measurement over Western Java Island, *Remote  
599 Sens. Appl. Soc. Environ.*, 29, 100885, <https://doi.org/10.1016/j.rsase.2022.100885>, 2023.

600 Ni, X., Liu, C., and Zipser, E.: Ice microphysical properties near the tops of deep convective cores implied by the GPM  
601 Dual-Frequency Radar observations, *J. Atmos. Sci.*, 76, 2899–2917, <https://doi.org/10.1175/JAS-D-18-0243.1>, 2019.

602 Peinó, E., Bech, J., Polls, F., Udina, M., Petracca, M., Adirosi, E., Gonzalez, S., and Boudevillain, B.: Validation of GPM  
603 DPR rainfall and drop size distributions using disdrometer observations in the Western Mediterranean, *Remote Sens.*, 16,  
604 2594, <https://doi.org/10.3390/rs16142594>, 2024.

605 Roy, P., Biswasharma, R., Deshamukhya, A., and Sharma, S.: Spatial and seasonal variation of rainfall contribution by the  
606 height spectrum of precipitation systems and associated cloud bulk properties over the South Asia, *Int. J. Climatol.*, 40,  
607 3771–3791, <https://doi.org/10.1002/joc.6427>, 2020.

608 Ryu, J., Song, H.-J., Sohn, B.-J., and Liu, C.: Global distribution of three types of drop size distribution representing heavy  
609 rainfall from GPM/DPR measurements, *Geophys. Res. Lett.*, 48, e2020GL090871, <https://doi.org/10.1029/2020GL090871>,  
610 2021.

611 Saha, P., Majumder, S., and Maitra, A.: Rain drop size distribution analysis at a tropical location near land-sea boundary,  
612 *Theor. Appl. Climatol.*, 147, 487–498, <https://doi.org/10.1007/s00704-021-03809-4>, 2022.

613 Seela, B. K., Janapati, J., Lin, P.-L., Wang, P. K., and Lee, M.-T.: Raindrop size distribution characteristics of summer and  
614 winter season rainfall over North Taiwan, *J. Geophys. Res. Atmos.*, 123, 11,602–11,624,  
615 <https://doi.org/10.1029/2018JD028307>, 2018.

616 Skofronick-Jackson, G., Petersen, W. A., Berg, W., Kidd, C., Stocker, E. F., Kirschbaum, D. B., Kakar, R., Braun, S. A.,  
617 Huffman, G. J., Iguchi, T., Kirtsetter, P. E., Kummerow, C., Meneghini, R., Oki, R., Olson, W. S., Takayabu, Y. N.,  
618 Furukawa, K., and Wilheit, T.: The global precipitation measurement (GPM) mission for science and society, *Bull. Amer.  
619 Meteor. Soc.*, 98, 1679–1695, <https://doi.org/10.1175/BAMS-D-15-00306.1>, 2017.

620 Snook, N. and Xue, M.: Effects of microphysical drop size distribution on tornadogenesis in supercell thunderstorms,  
621 *Geophys. Res. Lett.*, 35, <https://doi.org/10.1029/2008GL035866>, 2008.

622 Sowan, B., Hong, T.-P., Al-Qerem, A., Alauthman, M., and Matar, N.: Ensembling validation indices to estimate the optimal  
623 number of clusters, *Appl. Intell.*, 53, 9933–9957, <https://doi.org/10.1007/s10489-022-03939-w>, 2023.



624 Suh, S.-H., You, C.-H., and Lee, D.-I.: Climatological characteristics of raindrop size distributions in Busan, Republic of  
625 Korea, *Hydrol. Earth Syst. Sci.*, 20, 193–207, <https://doi.org/10.5194/hess-20-193-2016>, 2016.

626 Sun, Y., Dong, X., Cui, W., Zhou, Z., Fu, Z., Zhou, L., Deng, Y., and Cui, C.: Vertical structures of typical Meiyu  
627 precipitation events retrieved from GPM-DPR, *J. Geophys. Res. Atmos.*, 125, e2019JD031466,  
628 <https://doi.org/10.1029/2019JD031466>, 2020.

629 Tapiador, F. J., Turk, F. J., Petersen, W., Hou, A. Y., García-Ortega, E., Machado, L. A. T., Angelis, C. F., Salio, P., Kidd,  
630 C., Huffman, G. J., and de Castro, M.: Global precipitation measurement: Methods, datasets and applications, *Atmos. Res.*,  
631 104–105, 70–97, <https://doi.org/10.1016/j.atmosres.2011.10.021>, 2012.

632 Thompson, E. J., Rutledge, S. A., Dolan, B., and Thurai, M.: Drop size distributions and radar observations of convective  
633 and stratiform rain over the equatorial Indian and west Pacific Oceans, *J. Atmos. Sci.*, 72, 4091–4125,  
634 <https://doi.org/10.1175/JAS-D-14-0206.1>, 2015.

635 Uma, K. N. and Rao, T. N.: Characteristics of vertical velocity cores in different convective systems observed over Gadanki,  
636 India, *Mon. Weather Rev.*, 137, 954–975, <https://doi.org/10.1175/2008MWR2677.1>, 2009.

637 Wang, T. and Tang, G.: Spatial variability and linkage between extreme convections and extreme precipitation revealed by  
638 22-year space-borne precipitation radar data, *Geophys. Res. Lett.*, 47, e2020GL088437,  
639 <https://doi.org/10.1029/2020GL088437>, 2020.

640 Wen, J., Wang, G., Zhou, R., Li, R., Zhaxi, S., and Bai, M.: Seasonal variation in vertical structure for stratiform rain at  
641 Mêdog site in southeastern Tibetan Plateau, *Remote Sens.*, 16, 1230, <https://doi.org/10.3390/rs16071230>, 2024.

642 Wen, L., Chen, G., Yang, C., Zhang, H., and Fu, Z.: Seasonal variations in precipitation microphysics over East China based  
643 on GPM DPR observations, *Atmos. Res.*, 293, 106933, <https://doi.org/10.1016/j.atmosres.2023.106933>, 2023.

644 Wu, Z., Zhang, Y., Zhang, L., Zheng, H., and Huang, X.: A comparison of convective and stratiform precipitation  
645 microphysics of the record-breaking typhoon In-Fa (2021), *Remote Sens.*, 14, 344, <https://doi.org/10.3390/rs14020344>, 2022.

646 Zhang, Z., Li, H., Li, D., and Qi, Y.: Spatial variability of raindrop size distribution at Beijing city scale and its implications  
647 for polarimetric radar QPE, *Remote Sens.*, 15, 3964, <https://doi.org/10.3390/rs15163964>, 2023.